Non-linear finite element analyses applicable for the design of large reinforced concrete structures

M. Engen[a,b,*], M. A. N. Hendriks[b,c], J. A. Øverli[b] and E. Åldstedt[a]

[a]Multiconsult ASA, Postboks 265 Skøyen, 0213 Oslo, Norway; [b]Dept. of Structural Engineering, NTNU, Norwegian University of Science and Technology, Rich. Birkelandsvei 1A, 7491 Trondheim, Norway, [c]Faculty of Civil Engineering & Geosciences, Delft University of Technology, Steinweg 1, 2628CN Delft, The Netherlands

ARTICLE HISTORY
Compiled June 16, 2017

ABSTRACT
In order to make non-linear finite element analyses applicable during assessments of the ultimate load capacity or the structural reliability of large reinforced concrete structures, there is need for an efficient solution strategy with a low modelling uncertainty. A solution strategy comprises choices regarding force equilibrium, kinematic compatibility and constitutive relations. This contribution demonstrates four important steps in the process of developing a proper solution strategy: 1) definition, 2) verification by numerical experiments, 3) validation by benchmark analyses and 4) demonstration of applicability. A complete solution strategy is presented in detail, including a fully triaxial material model for concrete, which was adapted to facilitate its implementation in a standard finite element software. Insignificant sensitivity to finite element discretization, load step size, iteration method and convergence tolerance were found by numerical experiments. A low modelling uncertainty, denoted by the ratio of experimental to predicted capacity, was found by comparing the results from a range of experiments to results from non-linear finite element predictions. The applicability to large reinforced concrete structures is demonstrated by an analysis of an offshore concrete shell structure.

KEYWORDS
non-linear finite element analyses; large concrete shell structures; practical applications; ultimate load capacity; modelling uncertainty; structural design

1. Introduction

With the introduction of the semi-probabilistic safety formats in fib *Model Code 2010 for Concrete Structures* (*fib*, 2013), non-linear finite element analyses (NLFEA) are receiving increased interest from the engineering community. This paper addresses the topic of NLFEA applicable for the design of large reinforced concrete structures, where the main scope of the analyses are accurate predictions of the ultimate load capacity.

The design of large reinforced concrete shell structures like dams and offshore oil and gas platforms is normally based on global linear finite element analyses (LFEA). This allows for using the principle of superpositioning in order to handle the vast number of design load combinations (Brekke, Åldstedt, and Grosch, 1994; Engen, Hendriks,

*Corresponding author. E-mail: morten.engen@multiconsult.no

Øverli, and Åldstedt, 2015). For such large shell structures it is important to perform global analyses due to the interaction between global and local load effects. In order to reduce the computational cost, the finite elements are normally large compared to the sectional dimensions. Sufficient capacity is assured by performing local sectional design based on the sectional forces obtained from the LFEA.

In order to better take into account the real physical behaviour of reinforced concrete, non-linear finite element analyses (NLFEA) could be carried out in the design phase. The NLFEA should then be used in combination with methods for global reliability assessments, e.g. the semi-probabilistic safety formats suggested in fib *Model Code for Concrete Structures 2010* (*fib*, 2013). Due to cracking of concrete and yielding of reinforcement, a redistribution of the internal forces can be expected.

In order to perform NLFEA, the analyst needs to make proper choices regarding force equilibrium, kinematic compatibility and constitutive relations. Collectively, the choices constitute a strategy for obtaining a solution from NLFEA, or short, a *solution strategy* for NLFEA (Engen et al., 2015). Previous research has led to the development of a set of guidelines for NLFEA of reinforced or prestressed concrete beams, girders and slabs (Belletti, Damoni, and Hendriks, 2011; Belletti, Damoni, den Uijl, Hendriks, and Walraven, 2013; Belletti, Damoni, Hendriks, and de Boer, 2014; Belletti, Pimentel, Scolari, and Walraven, 2015; Hendriks, de Boer, and Belletti, 2017). However, the applicability to large reinforced concrete shell structures has not been demonstrated.

This contribution is part of an ongoing research project and complements the findings reported by the authors in two separate publications (Engen et al., 2015; Engen, Hendriks, Köhler, Øverli, and Åldstedt, 2017). Engen et al. (2015) compared results obtained with the mentioned guidelines to results reported elsewhere in the literature in order to select a solution strategy for further development. Engen et al. (2017) adapted the selected solution strategy and assessed the modelling uncertainty by comparing results obtained with NLFEA to experimental results reported in the literature. The modelling uncertainty can be defined as the ratio between the experimental and the predicted capacity, $\theta = R_{\text{exp}}/R_{\text{NLFEA}}$. The modelling uncertainty is mainly related to simplifications of the mathematical models compared to the real physical behaviour that is modelled, either for practical reasons or due to a lack of knowledge. This can be related to e.g. modelling of the material behaviour as a function of a limited number of variables, or a simplified representation of the real loading or boundary conditions. For reinforced concrete, the material model for concrete is considered the largest source of modelling uncertainties.

In this paper the selected solution strategy from Engen et al. (2015, 2017) is further developed and discussed in detail. The solution strategy includes a fully triaxial material model for concrete which was adapted to facilitate its implementation in a standard finite element software. The accuracy of the solution strategy should be assessed by verification and validation, where verification answers the question *are we solving the equations right?*, and validation answers the question *are we solving the right equations?* (Engen et al., 2017; Roache, 1998). The complete solution strategy was verified by comparing results obtained with different finite element discretizations, load step sizes and iterative solution procedures. Validation was performed by comparison of experimental and predicted results from a range of benchmark analyses. Results from two benchmark analyses are presented in this paper and the applicability to large concrete structures is demonstrated by NLFEA of an offshore concrete shell structure. It will be demonstrated that the ultimate load capacity and load-displacement relations can be efficiently predicted with reasonable accuracy in spite of using relatively simple material models and coarse finite element meshes. It should be noted that problems

related to e.g. durability or mechanical degradation, where a precise prediction of the crack pattern is important, might call for other and more detailed solution strategies.

2. Solution strategy for NLFEA

2.1. *Material model for concrete*

A common way of selecting material models for concrete is to use a uniaxial material model as basis, extended with additional models that take into account other material effects such as the effects of confinement and lateral cracking. Such an approach can be convenient when the structural effects of different material effects are to be studied, but additional models are normally developed in combination with other complementary models and should not be separated (Vecchio, 2001). Alternatively, fully triaxial material models where all material effects are treated, could be used. One such material model has been developed by Kotsovos and co-workers since the 1970s and is still subject to improvements (Bédard and Kotsovos, 1985; Cotsovos and Pavlovic, 2006; González Vidosa, Kotsovos, and Pavlovic, 1991a,b; Kotsovos, 1979a, 1980; Kotsovos and Pavlovic, 1995; Kotsovos and Spiliopoulos, 1998; Kotsovos, Pavlovic, and Cotsovos, 2008; Lykidis and Spiliopoulos, 2008; Markou and Papadrakakis, 2013; Spiliopoulos and Lykidis, 2006). Recently, the model was also adapted to light-weight aggregate concrete (Øverli, 2016). In the literature, it is stated that this model is particularly suited for structural engineering NLFEA. Demonstrations of the computational efficiency and comparisons to commercially available algorithms can be found in the literature (Bark, Markou, Mourlas, and Papadrakakis, 2016; Markou, Sabouni, Suleiman, and El-Chouli, 2015; Markou and Papadrakakis, 2013; Mourlas, Papadrakakis, and Markou, 2016).

The early versions of the fully triaxial material model are implemented in special purpose finite element software that allowed the user to interfer with the program on several levels. In order to make the material model available for practising engineers, it was adapted to facilitate its implementation in a standard finite element software in the present work. In the following, the basic ingredients, i.e. the constitutive relation and the fracture criterion, will be presented, the central parts of the implemented algorithms will be outlined and two improvements to the earlier versions of the model are highlighted.

In this section, the subscripts i and j are reserved for tensor components, while k and l are used for the load step and iteration number respectively. Thorough reviews of other constitutive relations and crack models for concrete can be found elsewhere (Cotsovos, 2004; González Vidosa, 1989; Rots, 1988; Rots and Blaauwendraad, 1989). It is emphasized that the objective of the present work was not to contribute to a detailed discussion about how concrete as a material *should* be modelled, but how it *could* be modelled in NLFEA performed by practising engineers where the purpose of the analysis is to assess the ultimate load capacity or structural reliability of large reinforced concrete structures. The material model did not include regularization of the constitutive relation in terms of e.g. crack bandwidth and fracture energy in order to obtain results that are objective with respect to the size of the finite elements (Bazant and Oh, 1983). It will be demonstrated that this sensitivity was insignificant when relatively large elements were used in analyses of reinforced concrete.

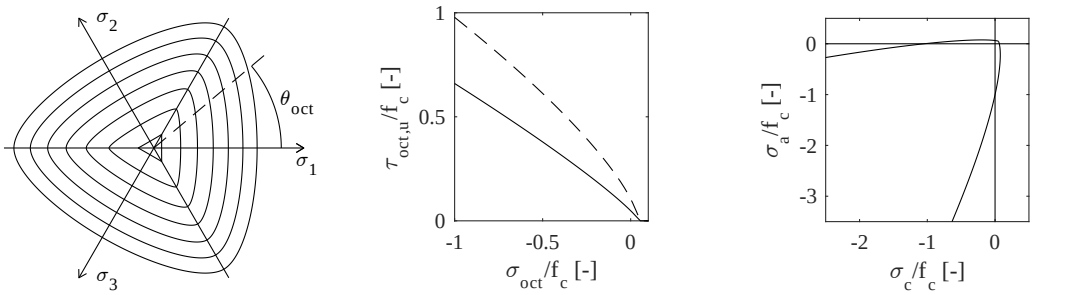

(a) Deviatoric sections of the fracture criterion for different levels of hydrostatic stress.

(b) $\tau_{\mathrm{oct,u}}$ for $\theta_{\mathrm{oct}} = 0°$ (solid) and $\theta_{\mathrm{oct}} = 60°$ (dashed).

(c) Hydrostatic section of the fracture criterion showing the axial strength σ_{a} as a function of the lateral confining stress σ_{c}.

Figure 1. Demonstration of the shape of the fracture criterion for concrete with $f_{\mathrm{c}} = 50$ MPa.

2.1.1. Constitutive relation and fracture criterion

When concrete is subjected to an increasing state of stress, the non-linear deformational response *below the ultimate stress level* can be described in terms of the internal fracture process which reduces tensile stress concentrations near the tips of internal microcracks (Kotsovos, 1979b). The response under multiaxial states of stress can be decomposed into three parts: 1) the change in volume due to hydrostatic loading, 2) the change of shape due to deviatoric loading and 3) the change in volume due to deviatoric loading (Kotsovos, 1980). Part 1 can be modelled by superimposing an internal hydrostatic stress, which is statically equivalent to the stress reduction due to microcracking, or by continuously degrading the bulk modulus, K, which is depending on the hydrostatic stress level. Similar reasoning can be used of parts 2 and 3. Due to this decomposition, it is convenient to decompose the stress state into octahedral stress components: σ_{oct}, τ_{oct} and θ_{oct}. σ_{oct} is the hydrostatic stress, which is the projection of the point in principal stress space onto the hydrostatic axis along $\sigma_1 = \sigma_2 = \sigma_3$. The deviatoric plane is orthogonal to the hydrostatic axis, and intersects with σ_{oct}. The point which represents the state of stress in principal stress space lies in the deviatoric plane with a distance τ_{oct} to the hydrostatic axis. θ_{oct} is the lode-angle which is the angle between the point in the deviatoric plane and the projection of the positive σ_1-axis as indicated in Figure 1(a). σ_{oct} is a function of the first invariant of the stress tensor, τ_{oct} is a function of the second invariant of the deviatoric stress tensor and θ_{oct} is a function of the second and third invariant of the deviatoric stress tensor.

By assuming non-linear elastic isotropic material behaviour for uncracked concrete and using the secant values of the stiffness moduli, the total strains corresponding to a given stress level below the ultimate stress level, can be calculated by Hooke's law in Equation (1) which can be interpreted as the sum of the change of shape and the change in volume.

$$\epsilon_{ij} = \frac{\sigma_{ij} - \sigma_{\mathrm{oct}}\delta_{ij}}{2G_{\mathrm{s}}} + \frac{(\sigma_{\mathrm{oct}} + \sigma_{\mathrm{id}})\delta_{ij}}{3K_{\mathrm{s}}} \tag{1}$$

G and K is the shear modulus and the bulk modulus, respectively. K and G represent part 1 and 2, respectively, of the non-linear deformational response described above. The subscript s indicates that the respective modulus is a secant modulus.

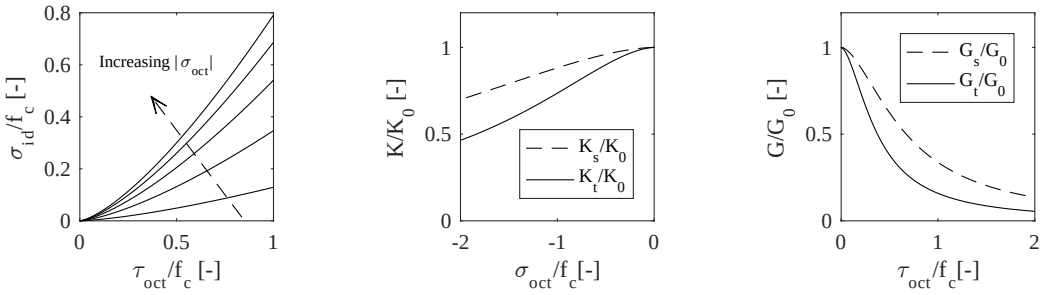

(a) Development of σ_{id} as a function of increasing deviatoric stress and compressive hydrostatic stress.

(b) Development of the bulk modulus as a function of increasing compressive hydrostatic stress.

(c) Development of the shear modulus as a function of increasing deviatoric stress.

Figure 2. Internal hydrostatic stress and non-linear bulk and shear moduli as functions of the stress level for concrete with $f_{\mathrm{c}} = 50$ MPa. The subscripts *0*, *s* and *t* indicate initial, secant and tangent values of the respective modulus.

σ_{id} is an equivalent internal hydrostatic stress which represents the change in volume due to deviatoric loading, i.e. part 3 of the non-linear deformational response, and is a function of the cylinder strength f_{c} and the current σ_{oct} and τ_{oct} (Kotsovos, 1980). The development of σ_{id} is shown in Figure 2(a). δ_{ij} is the *Kronecker delta* which is equal to unity for equal indices and zero elsewhere. Note that positive and negative values indicate tensile and compressive stresses and strains in the present work. With this type of formulation, the effects of confinement and *Poisson's ratio* on the stress-strain relation are automatically included. Initial, unloaded values of the shear and bulk modulus, G_0 and K_0, can be calculated from the cylinder strength, and expressions describing the dependency of the moduli on their initial values, the cylinder strength and the stress level are found in the literature (Kotsovos, 1980). Figures 2(b) and 2(c) show K and G respectively as functions of the stresses.

The ultimate stress level, given by a fracture criterion, is defined in terms of the critical octahedral shear stress, $\tau_{\mathrm{oct,u}}(\sigma_{\mathrm{oct}}, \theta_{\mathrm{oct}}, f_{\mathrm{c}})$, and expressions for $\tau_{\mathrm{oct,u}}$ dependent on σ_{oct}, θ_{oct} and f_{c} are found in the literature (Kotsovos, 1979a). The critical octahedral shear stresses for $\theta_{\mathrm{oct}} = 0^\circ$ and $\theta_{\mathrm{oct}} = 60^\circ$ are calculated using Equations (2) and (3) respectively, and shown in Figure 1(b). By ordering the principal stresses according to $\sigma_1 > \sigma_2 > \sigma_3$ it can be shown that all stress states have $0^\circ \leq \theta_{\mathrm{oct}} \leq 60^\circ$, and the relation proposed by Willam and Warnke (1974) can be used to calculate intermediate values of $\tau_{\mathrm{oct,u}}$ for given σ_{oct}, θ_{oct} and f_{c}. The fracture criterion can be interpreted as a limit beyond which the fracture process changes from internal microcracking to visible macrocracking. In the principal stress space, the fracture criterion can be visualized as a cone opening along the compressive hydrostatic axis, with a cross section approaching a triangle for hydrostatic tensile stresses, as demonstrated in Figure 1(a). Figure 1(c) demonstrates the significant effect of lateral stresses on the axial strength. If the fracture criterion is exceeded with at least one positive principal stress, a crack is formed on a plane with a normal parallel to the direction of the largest principal stress. If on the other hand the fracture criterion is exceeded with all principal stresses compressive, this corresponds to compressive failure, i.e. a complete loss of capacity in all directions.

$$\frac{\tau_{\mathrm{oct,u,0^\circ}}}{f_\mathrm{c}} = 0.633\left(0.05 - \frac{\sigma_\mathrm{oct}}{f_\mathrm{c}}\right)^{0.857} \tag{2}$$

$$\frac{\tau_{\mathrm{oct,u,60^\circ}}}{f_\mathrm{c}} = 0.944\left(0.05 - \frac{\sigma_\mathrm{oct}}{f_\mathrm{c}}\right)^{0.724} \tag{3}$$

Figure 3 shows the material response up to failure for a) uniaxial loading and b) 10% confining stresses. The effect of confinement on both deformations and capacity was a direct consequence of the stress-dependent non-linear stiffness moduli and fracture criterion. Following the approach presented in this section the material model depended on only one material parameter, the compressive cylinder strength. It is noted that the expressions for K, G, σ_id and $\tau_\mathrm{oct,u}$ found in the literature are results from fitting mathematical expressions to experimental results (Kotsovos, 1979a, 1980).

2.1.2. Outline of the implemented algorithm

The implemented material model consisted of three main parts: *A*) uncracked stress update algorithm, *B*) crack initiation and stress update algorithm for cracked integration points, and *C*) crack closing and stress update algorithm for closing integration points. Each part provided the appropriate material stiffness matrix. In part *A*, the non-linearities are mainly due to loading in compression, and in parts *B* and *C*, the non-linearities are due to opening and closing of cracks. Two improvements to the earlier versions of the material model were introduced: i) material stiffness matrix for uncracked integration points based on initial stiffness moduli, ii) and threshold angle for crack initiation.

A) Uncracked stress update algorithm. The stress-strain relationship up to the ultimate stress level given by Equation (1) is stress-driven, i.e. in the form $\boldsymbol{\epsilon} = \boldsymbol{\epsilon}(\boldsymbol{\sigma})$ where $\boldsymbol{\sigma}$ and $\boldsymbol{\epsilon}$ are the stress and strain vectors shown in Equation (4). Since typical strain-driven material models are required in standard finite element software, the relation should either be inverted or solved in an iterative manner. An iterative solution as proposed in the literature (González Vidosa, 1989; Kotsovos and Pavlovic, 1995) was used. In the iterative stress update, the fracture criterion was continuously monitored, and if $\tau_\mathrm{oct} > \tau_\mathrm{oct,u}$, $\tau_\mathrm{oct,u}$ was used in the calculation of G and σ_id in Equation (1). If this limitation was not used, G and σ_id could attain unrealistically low and high values respectively.

In a general case, the material stiffness matrix consists of partial derivatives of the constitutive relation in terms of the strains, or partial derivatives of the stress update algorithm in terms of the strains. Following the recommendations by Kotsovos and Pavlovic (1995) the material stiffness matrix, $\mathbf{C}$, was given in the form of Equation (5) corresponding to Hooke's law neglecting the coupling between deviatoric loading and hydrostatic deformation. The subscript t indicates that tangent stiffnesses were used, and $\lambda = K - 2G/3$ is *Lame's constant*. The material stiffness matrix according to Equation (5) with initial values for the material stiffness parameters was output from the material model. Compared to updated values for the stiffness parameters, this was found to have a slightly stiffening and stabilizing effect on the solution.

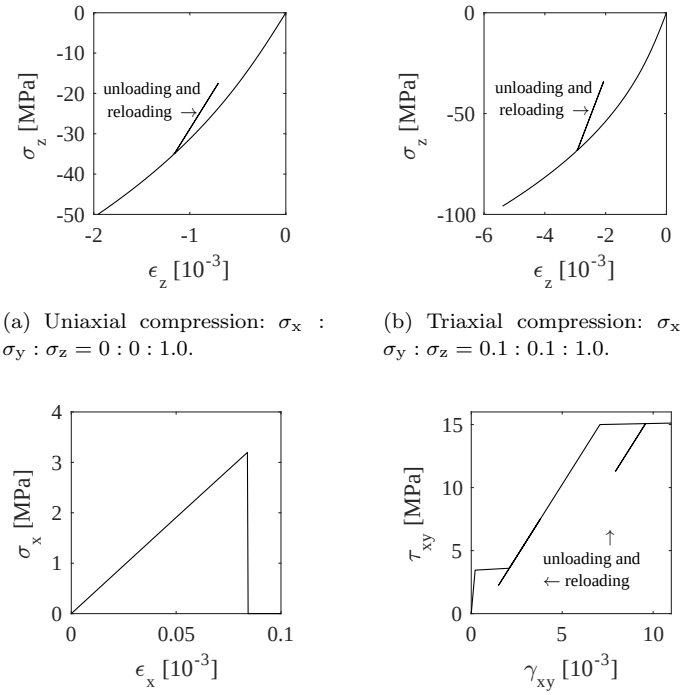

(a) Uniaxial compression: σ_x : $\sigma_y : \sigma_z = 0 : 0 : 1.0$.

(b) Triaxial compression: σ_x : $\sigma_y : \sigma_z = 0.1 : 0.1 : 1.0$.

(c) Uniaxial tension $\sigma_x > 0$.

(d) Pure shear $\tau_{xy} > 0$.

Figure 3. Examples of loading, unloading and reloading of concrete with $f_c = 50$ MPa subjected to a) uniaxial compression, b) triaxial compression, c) uniaxial tension and d) pure shear. Note that no unloading and reloading is shown for the uniaxial tension case and that reinforcement $\rho_x = \rho_y = 3\%$ with yield stress $f_y = 500$ MPa was included in the pure shear case.

$$\boldsymbol{\sigma} = \{\sigma_x \ \sigma_y \ \sigma_z \ \tau_{xy} \ \tau_{yz} \ \tau_{xz}\}^T \ , \ \boldsymbol{\epsilon} = \{\epsilon_x \ \epsilon_y \ \epsilon_z \ \gamma_{xy} \ \gamma_{yz} \ \gamma_{xz}\}^T \tag{4}$$

$$\mathbf{C} = \begin{bmatrix} 2G_t + \lambda_t & \lambda_t & \lambda_t & 0 & 0 & 0 \\ & 2G_t + \lambda_t & \lambda_t & 0 & 0 & 0 \\ & & 2G_t + \lambda_t & 0 & 0 & 0 \\ & & & G_t & 0 & 0 \\ & \text{sym.} & & & G_t & 0 \\ & & & & & G_t \end{bmatrix} \tag{5}$$

As indicated in Figure 2(c), the non-linearities due to deviatoric loading dominate, and τ_{oct} can be regarded as the main contributor to the internal fracture process below the ultimate stress level. τ_{oct} was thus used as an indicator for loading and unloading. If τ_{oct} was found to be less than the previously maximum sustained τ_{oct}, indicating unloading, the stresses were simply updated linearly using initial values of the material stiffness parameters as shown in the unloading-reloading branches in Figure 3. A similar procedure is suggested in the literature (Bathe, Walczak, Welch, and Mistry, 1989; Kotsovos, 1984; Kotsovos and Spiliopoulos, 1998). The resulting stress update for an uncracked integration point can be seen in Figure 3 for loading, unloading and reloading. It is evident that confinement leads to a stiffer material

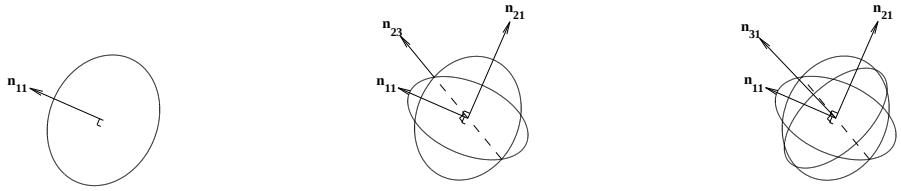

(a) One crack. The stress in the direction normal to the first crack plane, $\mathbf{n}_{11}$, is set to zero, and the stiffness is reduced.

(b) Two cracks. The stress in the direction of the intersection of the two crack planes, $\mathbf{n}_{23}$, is the only non-zero normal stress component.

(c) Three cracks. All normal stress components are set to zero.

Figure 4. Demonstration of possible crack states, where the plane of each open crack is visualized as a circle.

response, i.e. the strains are smaller in Figure 3(b) than in 3(a) for the same axial stress level, since due to a lower τ_{oct} the shear modulus is less degraded. Also, the axial stress at the ultimate stress level, and the corresponding strains are larger due to the stress dependent fracture criterion. If the confinement was further increased, the response would become more linear, but still non-linear due to the continuously degrading bulk modulus.

After the stresses were updated, the fracture criterion was checked, and if the stresses were found to exceed the ultimate stress level, i.e. if $\tau_{\text{oct}} > \tau_{\text{oct,u}}$, the crack initiation algorithm was called.

B) Crack initiation and cracked stress update algorithm. Upon cracking, the material model followed a smeared, non-orthogonal, fixed cracking approach with a maximum number of three cracks per integration point. The possible crack states are shown in Figure 4. In this context, the terms *fixed* and *non-orthogonal* refer to that the normal to a crack plane is kept constant after crack initiation and not rotated along the principal stress or strain directions, and that further cracking is not restricted to directions orthogonal to existing cracks. If the fracture criterion was exceeded with at least one principal tensile stress, a crack was initiated on a plane with a normal parallel to the largest principal stress, as shown by the vector $\mathbf{n}_{11}$ in Figure 4(a), resulting in a state of nearly plane stress. The stress normal to the crack plane was set equal to zero. If on the other hand the fracture criterion was exceeded with all principal stresses compressive, compressive failure was initiated by setting all normal stresses equal to zero, i.e. a complete loss of capacity in all directions. It should be noted that this way of treating cracking is non-standard as cracking is initiated in a brittle manner neglecting any softening both in tension and compression. Also, no measures were introduced on material level to ensure objectivity with respect to finite element size in terms of e.g. fracture energy and crack bandwidth (Bazant and Oh, 1983), but as will be demonstrated, the mesh size dependency was found to be insignificant for the coarse finite element meshes used in the present work.

$$\bar{\mathbf{C}}_1 = \begin{bmatrix} \beta_\sigma(2G_\mathrm{t}+\lambda_\mathrm{t}) & 0 & 0 & 0 & 0 & 0 \\ & 2G_\mathrm{t}+\lambda_\mathrm{t} & \lambda_\mathrm{t} & 0 & 0 & 0 \\ & & 2G_\mathrm{t}+\lambda_\mathrm{t} & 0 & 0 & 0 \\ & & & \beta_\tau G_\mathrm{t} & 0 & 0 \\ & \text{sym.} & & & G_\mathrm{t} & 0 \\ & & & & & \beta_\tau G_\mathrm{t} \end{bmatrix} \tag{6}$$

$$\bar{\mathbf{C}}_2 = \begin{bmatrix} \beta_\sigma(2G_\mathrm{t}+\lambda_\mathrm{t}) & 0 & 0 & 0 & 0 & 0 \\ & \beta_\sigma(2G_\mathrm{t}+\lambda_\mathrm{t}) & 0 & 0 & 0 & 0 \\ & & 2G_\mathrm{t}+\lambda_\mathrm{t} & 0 & 0 & 0 \\ & & & \beta_\tau G_\mathrm{t} & 0 & 0 \\ & \text{sym.} & & & \beta_\tau G_\mathrm{t} & 0 \\ & & & & & \beta_\tau G_\mathrm{t} \end{bmatrix} \tag{7}$$

$$\bar{\mathbf{C}}_3 = \begin{bmatrix} \beta_\sigma(2G_\mathrm{t}+\lambda_\mathrm{t}) & 0 & 0 & 0 & 0 & 0 \\ & \beta_\sigma(2G_\mathrm{t}+\lambda_\mathrm{t}) & 0 & 0 & 0 & 0 \\ & & \beta_\sigma(2G_\mathrm{t}+\lambda_\mathrm{t}) & 0 & 0 & 0 \\ & & & \beta_\tau G_\mathrm{t} & 0 & 0 \\ & \text{sym.} & & & \beta_\tau G_\mathrm{t} & 0 \\ & & & & & \beta_\tau G_\mathrm{t} \end{bmatrix} \tag{8}$$

The material stiffness matrix of a cracked integration point was evaluated in a local coordinate system defined by the crack direction, and transformed to global coordinates by an appropriate transformation rule. The stiffness parameters, G and λ, were assigned the values from the stress level upon first crack initiation, and kept constant for all remaining load steps regardless of further cracking and loading or unloading. The material stiffness matrix corresponding to one crack is given by Equation (6), which simply is a reduction of Equation (5), with the only remaining significant stiffnesses in the plane of the crack. The overbars in Equations (6) to (8) indicate that the matrices are established in a local coordinate system. The index *1* in Equation (6) indicates that the matrix represents one crack and that it is evaluated in the coordinate system defined by the vectors $\mathbf{n}_{11}$, $\mathbf{n}_{12}$ and $\mathbf{n}_{13}$, and similarly for the indices *2* and *3* in Equations (7) and (8). The normal retention factor, $\beta_\sigma = 0.0001$, followed the recommendations by Bathe et al. (1989), and was provided in order to avoid diagonal elements equal to zero. The shear retention factor, $\beta_\tau = 0.1$, followed the recommendations by Gonzlez Vidosa, Kotsovos, and Pavlovic (1988). It is emphasized that the off-diagonal terms that are set equal to zero in Equations (6) to (8) are equivalent to setting the corresponding Poisson's ratio equal to zero. This represents a simplified treatment of the gradual post-cracking reduction of the Poisson's ratio often recommended in the literature (Hendriks et al., 2017). The material stiffness matrix corresponding to compressive failure was set equal to the matrix corresponding to three cracks given by Equation (8).

When using a smeared crack approach, every crack represents an average crack state within the volume represented by the integration point. A rotation of the stress field and an increase of the stresses can lead to new cracks in the same integration point, but if the angle between the new and existing crack(s) is small, the new crack can

be interpreted as already represented by the existing crack(s), at least if the elements are relatively large. Hence, it is appropriate to introduce a *threshold angle* as a lower bound to the angle between the new and the existing crack(s). The effect of different values for the threshold angle between 0° and 90° is demonstrated in the literature (de Borst and Nauta, 1985; Rots and Blaauwendraad, 1989). A threshold angle of 45° was selected in the present work. Large threshold angles could lead to stress states exceeding the fracture criterion in critical integration points without initiating new cracks (de Borst and Nauta, 1985; Rots and Blaauwendraad, 1989). In order to ensure conservative results, this potential issue was avoided in the present work by proportionally scaling down the stress state in cases where the stresses exceeded the fracture criterion without initiating new cracks. The proportional stress scaling can be interpreted as a limitation of the stress state to a value given by the fracture criterion until new cracks are allowed to initiate.

If the fracture criterion was exceeded for the second time with at least one positive principal stress, a second crack could be formed on a plane with a normal parallel to the current largest principal stress, as indicated by the vector $\mathbf{n}_{21}$ in Figure 4(b). Note that $\mathbf{n}_{11}$ and $\mathbf{n}_{21}$ are non-orthogonal vectors separated by an angle larger than the threshold angle. The material stiffness matrix was reduced to Equation (7) with the only significant normal stiffness left in the direction of the intersection between the crack planes, indicated by the vector $\mathbf{n}_{23} = \mathbf{n}_{11} \times \mathbf{n}_{21}$ in Figure 4(b), resulting in a state of nearly uniaxial stress. The stresses in the directions $\mathbf{n}_{21}$ and $\mathbf{n}_{21} \times \mathbf{n}_{23}$ were set equal to zero. Finally, a third crack could be formed on a plane with a normal indicated by $\mathbf{n}_{31}$ in Figure 4(c) parallel to the current largest principal stress. With three cracks, the normal stresses in the directions corresponding to the principal stress directions upon formation of the third crack were all set equal to zero. The material stiffness matrix was given by Equation (8).

If the threshold angle was set equal to 0° and the stress scaling described above was left out, a possible outcome of initiating a new crack in a previously cracked integration point due to a small rotation of the stress field could be a spurious loss of capacity in a direction orthogonal to the normal to the new crack plane. Although not presented herein, the global results from analyses with values of the threshold angle below 45° showed no significant influence from the selected value, however, by introducing the threshold angle and the stress scaling, any potential spurious stress reduction was avoided.

The stress update of a cracked integration point followed a linear relation between the material stiffness matrices in Equations (6) to (8) and the total strain increment e.g. $\Delta\boldsymbol{\sigma} = \mathbf{C}_1\Delta\boldsymbol{\epsilon}$, where $\mathbf{C}_1$ is $\bar{\mathbf{C}}_1$ transformed to the global coordinate system, in addition to the stress reduction normal to the crack planes described above. The material stiffness matrices in Equations (6) to (8) are thus close approximations to the partial derivatives of the stress update algorithm, and will contribute to fast convergence. The resulting stress update is shown in Figures 3(c) and 3(d) for uniaxial tension and pure shear respectively. Before cracking in pure shear, the stresses are carried by the concrete as compression and tension in the principal directions. Upon cracking, the principal tensile stress is reduced to zero, and the concrete carries stresses in principal compression only, resulting in stresses in the coordinate directions that need to be equilibrated by reinforcement. Hence, the results for pure shear were obtained with reinforcement amounts $\rho_{\mathrm{x}} = \rho_{\mathrm{y}} = 3\%$ and a yield stress $f_{\mathrm{y}} = 500$ MPa.

C) Crack closing and closing stress update algorithm. In a cracked integration point, the strain(s) normal to the crack plane(s) were checked. If the total strain normal to a crack plane was found to turn negative, and less than its value upon cracking, the

crack was in a state of closing. It should be noted that the strain upon cracking could be negative if the integration point was unloading to cracking from a compressive state of stress.

The material stiffness matrix was restored for the appropriate number of cracks that remained open and evaluated locally according to the directions of the remaining crack(s). An integration point that had experienced compressive failure was not allowed to close, since compressive failure represented a complete loss of capacity in all directions.

The stresses in a closing integration point were first updated according to the algorithm for cracked integration points. If one crack was found to be closing, the total strains were transformed to the local directions of the closing crack and multiplied with a uniaxial stiffness in order to find the stresses due to closing, $\Delta\bar{\boldsymbol{\sigma}}$, according to Equation (9). The local closing stress was further transformed to global coordinates and added to the current stress. A similar procedure was applied to two and three closing cracks with plane stress and triaxial stiffnesses respectively, according to Equations (10) and (11). In Equations (9) to (11), the overbars indicate that the stresses and strains are transformed to local coordinates and the numerical subscripts indicate strains along the first, second and third local axis. By following this procedure it was ensured that the closing stress update was unified with the cracked stress update and that the correct stress components were updated for closing. This algorithm is similar to what was presented by Spiliopoulos and Lykidis (2006).

$$\Delta\bar{\sigma}_{\text{uniaxial}} = \frac{G_{\text{t}}(2G_{\text{t}} + 3\lambda_{\text{t}})}{G_{\text{t}} + \lambda_{\text{t}}}\bar{\epsilon}_1 \rightarrow \Delta\bar{\boldsymbol{\sigma}} = \begin{Bmatrix} \Delta\bar{\sigma}_{\text{uniaxial}} \\ 0 \\ 0 \\ 0 \\ 0 \\ 0 \end{Bmatrix} \tag{9}$$

$$\Delta\bar{\boldsymbol{\sigma}}_{\text{plane}} = \begin{bmatrix} \dfrac{4G_{\text{t}}(G_{\text{t}} + \lambda_{\text{t}})}{2G_{\text{t}} + \lambda_{\text{t}}} & \dfrac{2G_{\text{t}}\lambda_{\text{t}}}{2G_{\text{t}} + \lambda_{\text{t}}} \\ \text{sym.} & \dfrac{4G_{\text{t}}(G_{\text{t}} + \lambda_{\text{t}})}{2G_{\text{t}} + \lambda_{\text{t}}} \end{bmatrix} \begin{Bmatrix} \bar{\epsilon}_1 \\ \bar{\epsilon}_2 \end{Bmatrix} \rightarrow \Delta\bar{\boldsymbol{\sigma}} = \begin{Bmatrix} \Delta\bar{\boldsymbol{\sigma}}_{\text{plane}} \\ 0 \\ 0 \\ 0 \\ 0 \end{Bmatrix} \tag{10}$$

$$\Delta\bar{\boldsymbol{\sigma}}_{\text{triaxial}} = \begin{bmatrix} 2G_{\text{t}} + \lambda_{\text{t}} & \lambda_{\text{t}} & \lambda_{\text{t}} \\ & 2G_{\text{t}} + \lambda_{\text{t}} & \lambda_{\text{t}} \\ \text{sym.} & & 2G_{\text{t}} + \lambda_{\text{t}} \end{bmatrix} \begin{Bmatrix} \bar{\epsilon}_1 \\ \bar{\epsilon}_2 \\ \bar{\epsilon}_3 \end{Bmatrix} \rightarrow \Delta\bar{\boldsymbol{\sigma}} = \begin{Bmatrix} \Delta\bar{\boldsymbol{\sigma}}_{\text{triaxial}} \\ 0 \\ 0 \\ 0 \end{Bmatrix} \tag{11}$$

2.2. *Material model for reinforcement*

A bilinear elastic-plastic relation was used for the reinforcement. The initial slope of the stress-strain curve was fully defined by an elastic Young's modulus $E = 200000$ MPa. After yielding, the relation between stress and total strain was defined by a low hard-

ening modulus $E_{\mathrm{H}} = 2000$ MPa. Similar recommendations are found in the literature (Hendriks et al., 2017; Kotsovos and Pavlovic, 1995).

2.3. *Force equilibrium*

In the present work, results from analyses with modified and full Newton-Raphson were compared. Line search was applied in order to improve the iterative displacement increments. For reinforced concrete structures, a force based convergence criterion can be difficult, or even impossible, to satisfy in load steps where large forces need to be redistributed due to cracking. This is expected to be pronounced in analyses with large elements and large load steps. In the present work, a force criterion based on the change in the norm of the nodal residual forces given by Equation (12) was thus used in combination with an energy criterion given by Equation (13). $\mathbf{R}_{\mathrm{res}}$ is the vector of nodal residual forces, $\delta\mathbf{u}$ is the vector of nodal iterative displacement increments, and ϵ_{F} and ϵ_{E} are the convergence tolerances. The subscripts *l*, *1* and *0* indicate the current iteration, the first iteration of the current load step, and the last iteration of the previous load step respectively. According to recommendations published elsewhere (Hendriks et al., 2017) the tolerances were set to $\epsilon_{\mathrm{F}} = 0.01$ and $\epsilon_{\mathrm{E}} = 0.001$. Convergence was achieved with at least one of the criteria satisfied within a maximum number of 40 iterations per load step. The load was applied with constant load increments.

$$\frac{|\sqrt{\mathbf{R}_{\mathrm{res},l}^T\mathbf{R}_{\mathrm{res},l}} - \sqrt{\mathbf{R}_{\mathrm{res},l-1}^T\mathbf{R}_{\mathrm{res},l-1}}|}{|\sqrt{\mathbf{R}_{\mathrm{res},1}^T\mathbf{R}_{\mathrm{res},1}} - \sqrt{\mathbf{R}_{\mathrm{res},0}^T\mathbf{R}_{\mathrm{res},0}}|} \leq \epsilon_{\mathrm{F}} \tag{12}$$

$$\frac{\delta\mathbf{u}_l^T\mathbf{R}_{\mathrm{res},l}}{\delta\mathbf{u}_1^T\mathbf{R}_{\mathrm{res},1}} \leq \epsilon_{\mathrm{E}} \tag{13}$$

2.4. *Kinematic compatibility*

When analysing concrete shell structures, shell elements are often preferred due to their efficiency in modelling and computation. However, such elements usually require additional capacity control, since the interaction between in-plane forces and moments, and transverse shear forces is usually not accounted for in the NLFEA. Solid elements thus seem most applicable. This also allows the analyst to model the geometry and load application more accurately, and ensures correct modelling of the stiffness in structural joints. In LFEA with properly formulated hexahedral elements, the internal forces and bending moments in slender shells can be calculated with high accuracy even with only one element over the shell thickness or beam height. However, in NLFEA it is expected that there is need for evaluation of the internal stress state in a larger number of integration points over the thickness in order to capture the effect of cracking, and the interaction between in-plane forces, bending moments and transverse shear forces.

Markou and Papadrakakis (2013) have stated that the use of numerically unstable material models is one of the reasons for researchers to use higher order elements with higher order numerical integration rules. Bergan and Holand (1979) argues that higher order interpolation functions with artificially high differentiability should be avoided

due to the highly discrete and localized deformational behaviour of concrete. This is considered particularly relevant in analyses with relatively large finite elements, i.e. elements that are large relative to the cross sectional dimensions. Artificial straining should also be avoided in order to reduce the risk of premature cracking. The two-point Gauss rule calculates the exact values of stresses and strains for undistorted elements (Barlow, 1976), and the error is smaller with a two-point rule than with a three-point rule in case of distorted elements (Barlow, 1989). This was believed to be crucial in the present work in order to reduce artificial straining and the risk of premature cracking.

Based on these arguments, fully integrated *8-noded solid elements* were used in the present work. In order to avoid spurious shear strains in bending dominated areas, so-called *enhanced strains* were used (Simo and Rifai, 1990; Simo, Armero, and Taylor, 1993). A minimum number of three elements were used over the shell thickness or beam height. Compared to using *20-* or *27-noded solid elements* the size of the global stiffness matrix can be significantly reduced which in turn results in a faster solution of each equilibrium iteration and a lower amount of required memory.

The reinforcement was assumed fully bonded, i.e. neglecting any differential deformation between the concrete and the reinforcement. This assumption was justified by the size of the elements, prohibiting any detailed modelling of local variations in the interface. The reinforcement was modelled as elements overlaying the solid concrete elements, providing strength and stiffness embedded within the volume of the concrete element according to the material model of the reinforcement steel, the cross sectional area of the bars, the orientation in space and the size of the cover. This functionality, referred to as embedded reinforcement in most commercial finite element software, is an efficient way of modelling reinforcement in engineering applications, without the need for adapting the mesh of solid elements to the reinforcement layout.

3. Verification by numerical experiments

Verification is related to how the mathematical problem is solved, and the sensitivity to the selected solution method. The sensitivity to size of finite elements, Newton-Raphson procedure and size of load steps were assessed by performing numerical experiments of two setups that were designed for the purpose. In the crack plots of this section and Section 5, each crack is visualized as a circular plane with a normal parallel to the largest principal tensile stress upon cracking. If the normal lies in the drawing plane, the crack appears as a line, but if the normal forms an angle with the drawing plane, the crack appears as an ellipse approaching a circle. If the crack closes, the symbol is removed, and the integration point appears as uncracked in the figure.

3.1. *Description of the numerical experiment setups*

One *slender* and one *short* beam was designed for the verification of the solution strategy. The cross section and reinforcement layout is shown in Figure 5(a). The concrete had a cylinder strength of 40 MPa and all reinforcement had a yield strength of 500 MPa. The slender and the short beam had a total length of 6 m and 3 m respectively. The beams were simply supported and were subjected to a constant distributed load, as shown schematically in Figure 5(b). Unless explicitly specified, the load steps were adjusted in order to reach yielding of the tensile reinforcement after 30 load steps. In the Figures 6, 9 and 10 the total load, $R = R_1 + R_2$, is plotted against the vertical displacement, Δ, at the midspan.

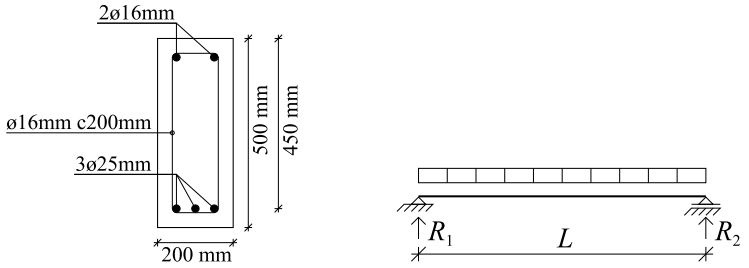

(a) Cross section. (b) Loading and boundary conditions.

Figure 5. Details of the numerical experiment setups.

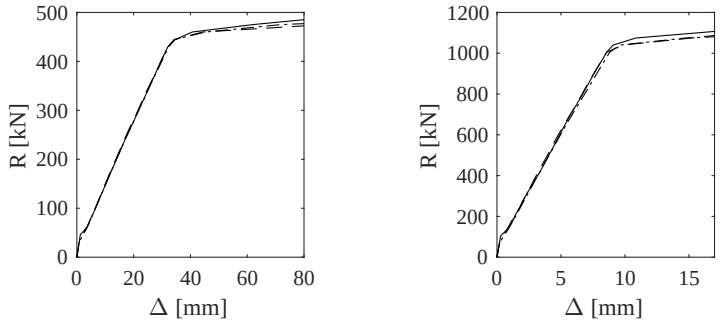

(a) Slender case. (b) Short case.

Figure 6. Comparison of results obtained with modified Newton-Raphson with three (solid), six (dashed) and nine (dash-dotted) elements over the beam height for a) slender case and b) short case.

3.2. *Sensitivity to size of finite elements*

The sensitivity to finite element discretization was checked by performing analyses of the two experimental setups with three different element sizes. Three, six and nine elements were used over the beam height, and the number of elements along the beam length was adjusted in order to keep the elements square. Two elements were used over the width in all analyses. Figure 6 shows the resulting load-displacement curves from analyses with modified Newton-Raphson, and no significant element size dependency can be observed. Similar results were obtained with full Newton-Raphson. Figures 7 and 8 show examples of the resulting crack patterns. For each load level, the crack directions were comparable. The element size in the coarsest meshes was comparable to the crack spacing that can by estimated using e.g. fib *Model Code 2010* (*fib*, 2013). The observed cracks in the results from the analyses with the coarsest meshes should thus be interpreted as average states of cracking within the volume corresponding to each integration point. With smaller elements, it can be seen that the crack patterns were gradually localizing, and the crack spacing can be found as a result of the analysis. This topic of gaining more details from the results upon mesh refinement has been elaborated on in the literature (*fib*, 2008), but will not be taken further here. As the mesh was refined, the cracks were found to propagate deeper towards the compressive zone, although this had no significant effect on the load-displacement curves as shown in Figure 6. The coarsest meshes in Figures 7 and 8 are comparable to the element sizes that were used in the validation in Section 4 and the demonstrations in Section 5.

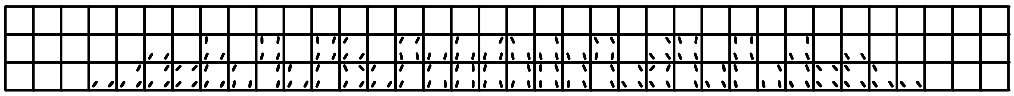

(a) Three elements over the beam height.

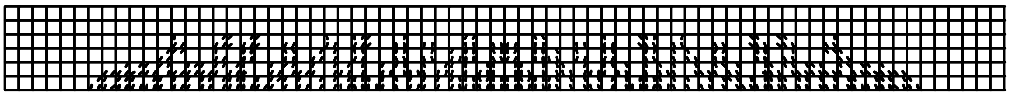

(b) Six elements over the beam height.

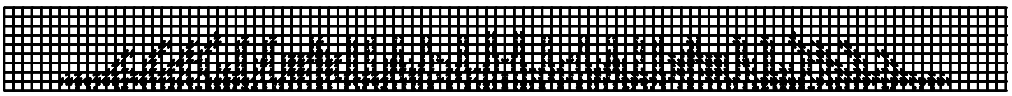

(c) Nine elements over the beam height.

Figure 7. Crack patterns for the slender case at load step 10: $R = 153$ kN. All the analyses were performed with two elements over the width of the beam.

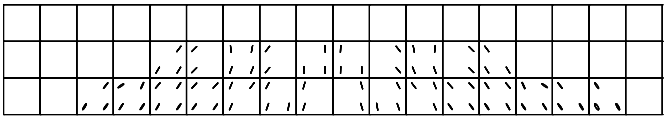

(a) Three elements over the beam height.

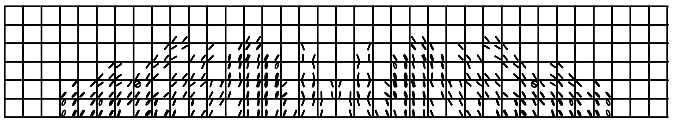

(b) Six elements over the beam height.

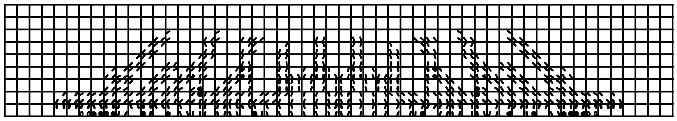

(c) Nine elements over the beam height.

Figure 8. Crack patterns for the short case at load step 10: $R = 347$ kN. All the analyses were performed with two elements over the width of the beam.

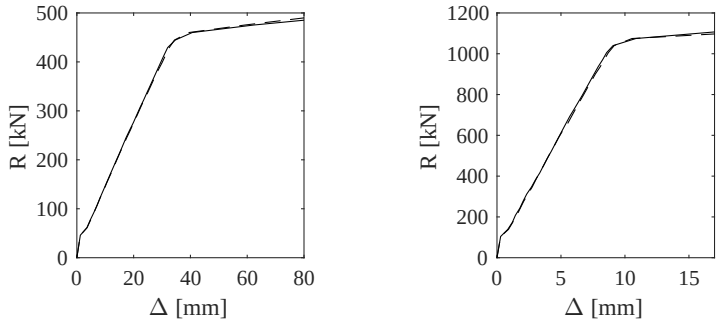

(a) Slender case. (b) Short case.

Figure 9. Comparison of results obtained with three elements over the beam height with modified (solid) and full (dashed) Newton-Raphson for a) slender case and b) short case.

3.3. *Sensitivity to Newton-Raphson procedure*

The sensitivity to the method for updating the tangent stiffness matrix during equilibrium iterations was checked by comparing results from analyses with full and modified Newton-Raphson. All of the analyses were performed with three elements over the beam height. The resulting load-displacement curves are shown in Figure 9. No significant sensitivity was observed in either of the cases. For the slender case, a total number of 409 iterations with modified Newton-Raphson taking approximately 115 s was needed to reach yielding of the longitudinal reinforcement in 30 load steps. These numbers were reduced to 214 iterations and 60 s using full Newton Raphson. Similarly for the short case, 277 iterations in 40 s and 173 iterations in 30 s was needed with modified and full Newton-Raphson respectively. A slight increase of the calculation time per iteration with full Newton-Raphson was thus compensated for by requiring a lower number of iterations for reaching convergence. The sensitivity to the selected convergence tolerances were also assessed by decreasing the tolerance of the force-based convergence criterion, however no significant influence on the resulting load-displacement curve could be observed.

3.4. *Sensitivity to size of load steps*

The sensitivity to the size of the load steps was checked by performing analyses of both the slender and the short case with three elements over the beam height, modified Newton-Raphson and applying the load corresponding to yielding of the longitudinal reinforcement in 30, 20 and ten load steps. The resulting load-displacement curves are shown in Figure 10, where no significant sensitivity can be observed.

4. Validation by benchmark analyses

Validation is related to how well the numerical predictions correspond to real observations. In the present work, validation was performed by comparing experimental and predicted capacities from 38 benchmark analyses. The sample of benchmark analyses contained beams (Bresler and Scordelis, 1963; Jelic, Pavlovic, and Kotsovos, 2004; Kotsovos, 1982), walls (Cervenka and Gerstle, 1972; Lefas, Kotsovos, and Ambraseys, 1990) and frames (Ernst, Smith, Riveland, and Pierce, 1973; Vecchio and Balopoulou,

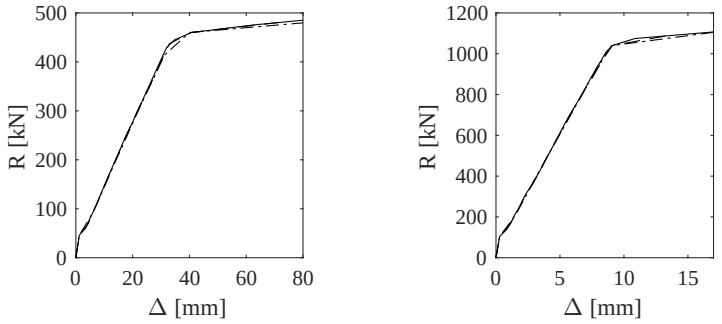

(a) Slender case. (b) Short case.

Figure 10. Comparison of results obtained with modified Newton-Raphson and three elements over the beam height with 30 (solid), 20 (dashed) and ten (dash-dotted) load steps for a) slender case and b) short case.

1990; Vecchio and Emara, 1992) with failure modes ranging from fully brittle to fully ductile. The sample could have been separated in smaller samples depending on the failure mode or type of structural component, but since the failure mode of large concrete shell structures most likely is due to an interaction between different sectional forces, the collection seems justified. During post-processing of the results from the benchmark analyses, the nodal displacement increments were plotted as deformed shapes, and if the displacement increments were found to significantly change from step to step, this was treated as a warning of failure. The last converged load step before failure was selected as the predicted capacity. Failure can thus be interpreted as the load level where the materials are degraded to such an extent, either due to cracking, yielding or both, that a further internal redistribution of forces is not possible.

Figure 11 shows the relation between experimental and predicted capacity. It is evident that the capacity is properly predicted with a small scatter in most of the cases. Based on these results, the modelling uncertainty, $\theta = R_{\text{exp}}/R_{\text{NLFEA}}$ can be assessed. By using the Bayesian inference technique suggested by (Engen et al., 2017) and assuming that θ can be modelled as a log-normally distributed random variable, a mean $\mu_\theta = 1.07$ and a coefficient of variation $V_\theta = 0.09$ was found. This can be regarded as being within the requirements suggested in the literature (Pimentel, Brühwiler, and Figueiras, 2014; Schlune, Plos, and Gylltoft, 2012). Engen et al. (2017) analysed the same set of benchmark experiments with the same solution strategy as used herein, however using modified Newton-Raphson, a force-based convergence criterion, $||\mathbf{R}_{\text{res}}||/||\mathbf{R}_{\text{ext}}|| < 0.01$, and not continuously monitoring the fracture criterion during the stress update algorithm for uncracked integration points as mentioned in Section 2.1.2. $\mathbf{R}_{\text{res}}$ is the vector of nodal residual forces, $\mathbf{R}_{\text{ext}}$ is the vector of nodal external loads, and $||\cdot||$ is the L_2-norm of the vectors. With these settings, $\mu_\theta = 1.10$ and $V_\theta = 0.11$ was obtained. Assuming a 5% level of significance, the modelling uncertainty obtained using the two versions of the solution strategy can not be rejected to come from the same population, i.e. having the same mean and coefficient of variation. This finding underlines the conclusions from the previous section where no sensitivity to Newton-Raphson procedure was found.

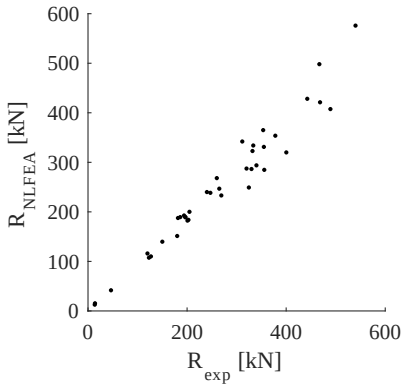

Figure 11. Predicted and experimental capacities, R_{NLFEA} and R_{exp}, for the 38 benchmark analyses.

Table 1. Summary of computational performance in the three demonstration cases.

Case	Solid elements	Reinf. elements	Equations	Iterations	Solution time
MDCB3	162	378	974	763	178 s
2D18H	720	1764	4286	775	764 s
Large structure	5547	10554	22351	662	3965 s

5. Demonstration of performance

In this section, the performance of the solution strategy is demonstrated by two benchmark analyses from the previous section involving sequential loading and an analysis of an offshore concrete shell structure that was specially designed in the present work. The focus of the present work was on the structural behaviour at the ultimate load level, and the presented results were thus limited to load-displacement curves and crack plots for the benchmark analyses and displacement plots and indications of internal load redistributions for the shell structure. It is noted again that all of the analyses were performed using solid elements.

Table 1 shows a summary of the number of elements, equilibrium equations, total number of iterations and the time spent computing the solutions of the NLFEA in this section. All analyses were performed on a Windows PC with an Intel Xeon E5620 CPU with 2.39 GHz and 16 GB RAM. No parallel processing was used. The average solution time per iteration and equilibrium equation was 0.23 ms to 0.27 ms in all analyses. This number should only be treated as indicative, since the solution time highly depends on the computer specifications and how data are transferred by the solver.

5.1. *Continuous beam MDCB3 by* Jelic, Pavlovic & Kotsovos

Jelic et al. (2004) tested simply supported beams subjected to sequential loading. The beam MDCB3 was selected for the present paper. The loading and supports are shown schematically in Figure 12(b), where the loads R_1 and R_2 were applied as pressures over the full width and two elements along the length, and the supports were modelled by multi-point constraints in order to mimic the load and support plates. The load at the midspan, R_1, was applied first, and while keeping $R_1 = 90$ kN, the load at the tip of the cantilever, R_2, was increased until failure. R_2 was applied with constant load steps so that the experimental capacity of $R_2 = 103.9$ kN was reached in 30 load

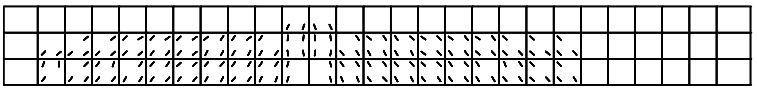

(a) Full intensity of the load at midspan: $R_1 = 90$ kN, $R_2 = 0$ kN.

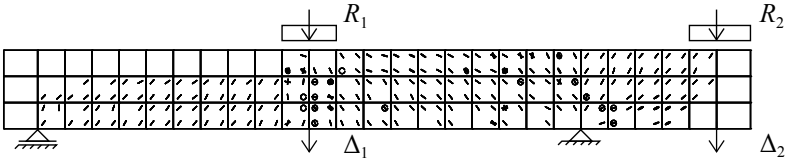

(b) Load step 2 substep 30: $R_1 + R_2 = 192.6$ kN.

Figure 12. Crack patterns for the beam MDCB3 tested by Jelic et al. for a) full intensity of the load at midspan and b) failure. The analysis was performed with two elements over the width of the beam.

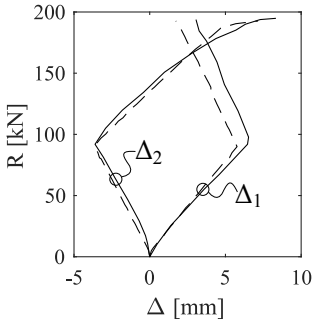

(a) Experimental and predicted load-displacement curve for the beam MDCB3 tested by Jelic et al.

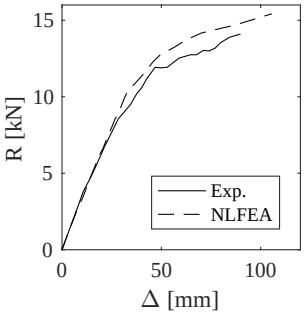

(b) Experimental and predicted load-displacement curves for the frame 2D18H tested by Ernst et al.

Figure 13. Load-displacement curves from the two benchmark analyses.

steps. The predicted total failure load was $R_{\mathrm{NLFEA}} = R_1 + R_2 = 192.6$ kN, giving a modelling uncertainty $\theta = 1.01$. The resulting load-displacement curve is shown in Figure 13(a) where the total reaction is plotted against the deflections below the two point loads. Crack patterns for selected load steps are shown in Figure 12, where it can be seen that several cracks were closing during application of the second point load. The predicted failure mode was characterized by diagonal cracking between the point load at the tip of the cantilever and the right support, combined with yielding of the longitudinal reinforcement over the support, corresponding to the failure mode described by Jelic et al. (2004).

5.2. *Portal frame 2D18H by* Ernst, Smith, Riveland & Pierce

Ernst et al. (1973) tested the portal frame 2D18H subjected to three vertical point loads and one horizontal point load. While keeping the total vertical load constant with a value $3V = 24.6$ kN, the horizontal load, R, was increased until failure. The loading and supports are shown schematically in Figure 14(b), where the horizontal and vertical loads were applied as distributed pressures over three and two elements along the height and length respectively, and the supports were modelled by multi-point constraints in order to mimic the load and support plates. R was applied with constant load steps so that the experimental capacity of $R = 14.1$ kN was reached in

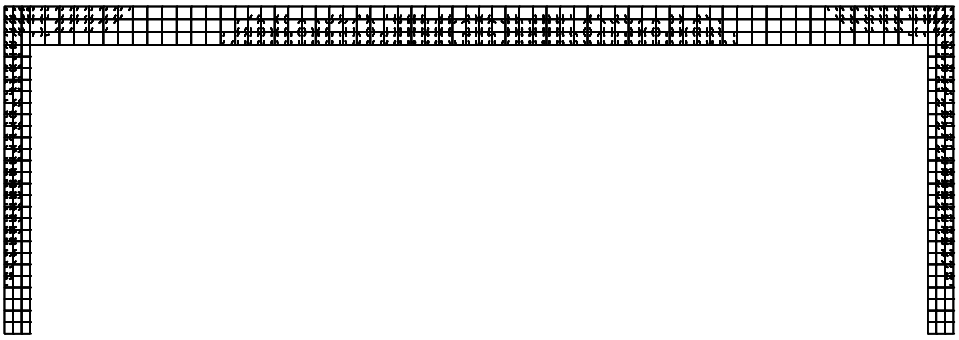

(a) Full intensity of the vertical loads: $V = 8.2$ kN, $R = 0$.

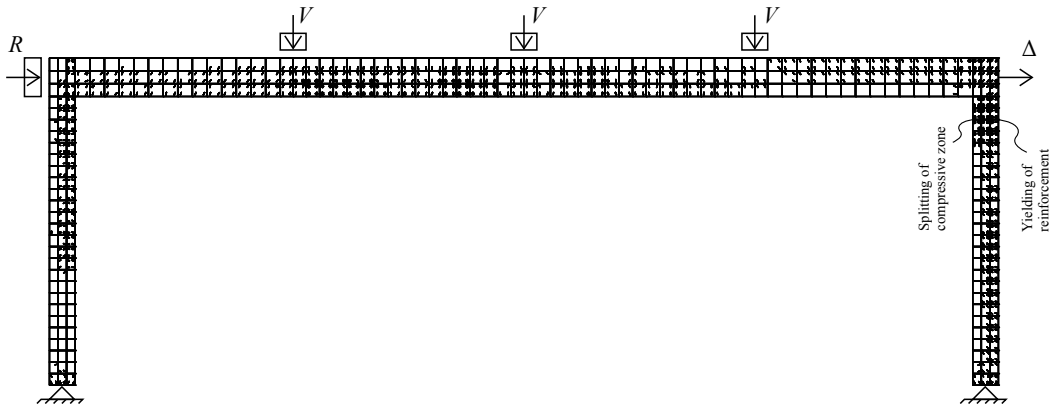

(b) Load step 2 substep 32: $V = 8.2$ kN, $R = 15.4$ kN.

Figure 14. Crack patterns for the frame 2D18H tested by Ernst et al. for a) full intensity of the vertical loads and b) failure. The analysis was performed with two elements over the width of the cross sections.

30 load steps. The predicted failure load was $R_{\mathrm{NLFEA}} = 15.4$ kN, giving $\theta = 0.92$. The resulting load-displacement curve is shown in Figure 13(b), where the total horizontal reaction is plotted against the horizontal deflection at the top. Crack plots for selected load steps are shown in Figure 14. Due to the reversed bending in the left leg of the frame resulting from application of the horizontal load, several cracks were closing when approaching the ultimate load level. The predicted failure mode was characterized by yielding of the outer longitudinal reinforcement of the right leg, followed by splitting of the compressive zone in the inner right corner and compressive failure, in close agreement with what was reported by Ernst et al. (1973).

5.3. *Offshore concrete shell structure*

A large offshore concrete shell structure suitable for oil or gas production was specially designed during this work. A thorough description of e.g. the design procedure, resulting reinforcement layout and geometry is beyond the scope of this paper, and only a brief description is provided in the following. A description of the design, construction and performance of offshore concrete structures for oil and gas fields can be found in the literature (*fib*, 2009).

The structure consisted of a 90 m tall shaft supported on a 10 m tall circular caisson as shown in Figure 15(a). The outer radii of the shaft and caisson were 6 m and 18 m respectively. The purpose of the structure is to support a topside with production

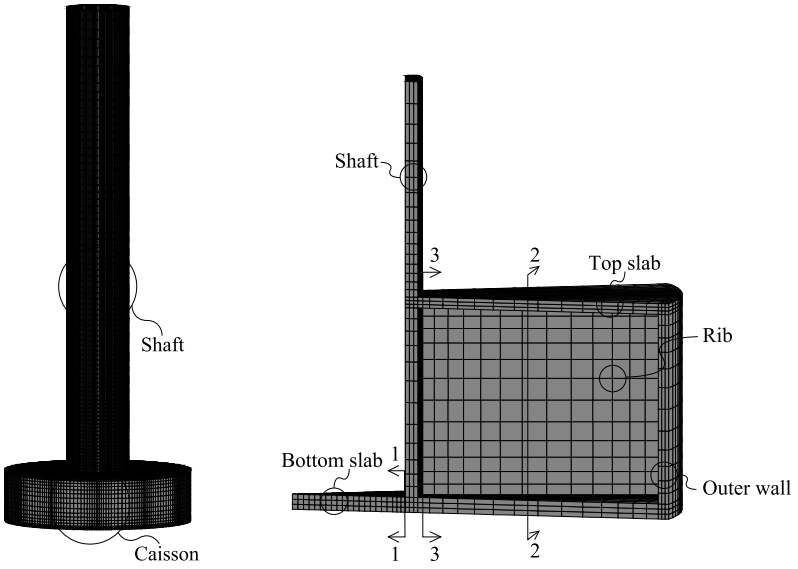

(a) Complete structure.

(b) The sector covering 30° and a total height of 20 m which was studied in the present work.

Figure 15. Offshore concrete structure.

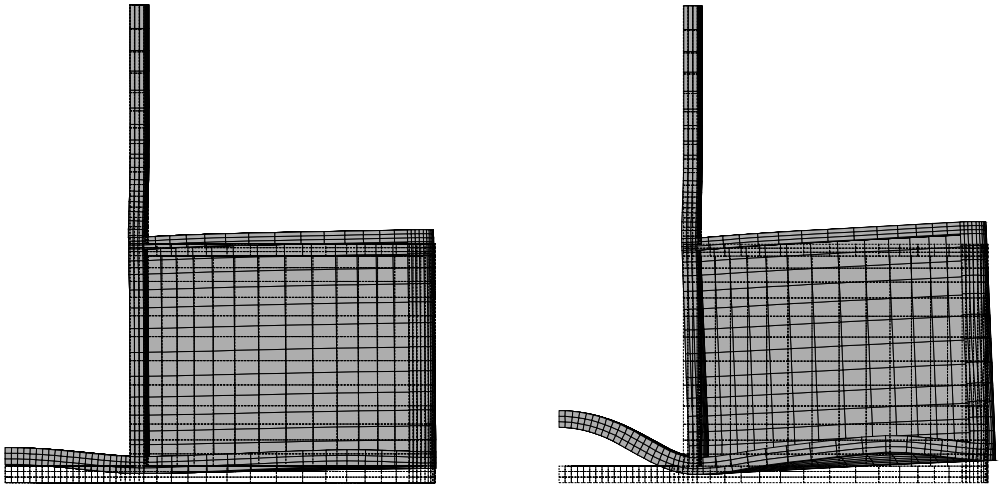

(a) LFEA.

(b) NLFEA.

Figure 16. Deformed shape at full characteristic intensity of all applied loads. The displacements are scaled with a factor of 100.

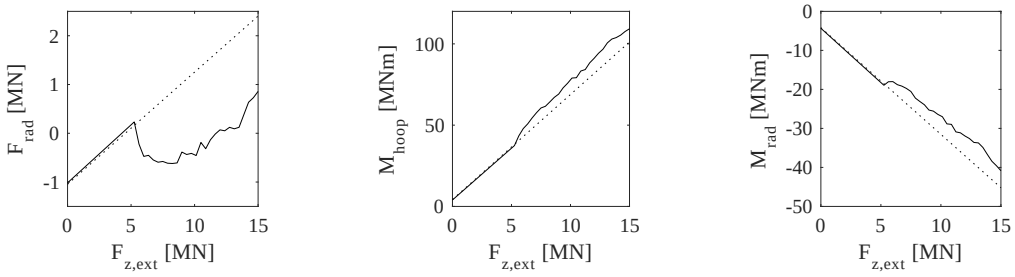

(a) Radial force resultant in the bottom slab in section 1-1, F_{rad}.

(b) Global bending moment in the caisson in hoop direction in section 2-2, M_{hoop}.

(c) Global bending moment in the caisson in radial direction in section 3-3, M_{rad}.

Figure 17. Force resultants and global bending moments in sections as functions of the total applied load from the topside carried by the studied part of the structure, $F_{\mathrm{z,ext}}$, from NLFEA (solid) and LFEA (dotted). The bending moments are calculated around the mid-height of the caisson, and the sections are shown in Figure 15(b).

facilities and living quarters with an assumed total weight of 18000 t, and to guide riser pipes from the sea-bed through the caisson and shaft. A mean water depth of 80 m was assumed to be applicable, and the structure was assumed to be completely waterfilled during operation. The caisson was stiffened with twelve equally spaced ribs as shown in Figure 15(b). A concrete strength of B55 and reinforcement steel strength of B500NC according to NS 3473 (Norges Standardiseringsforbund, 2003) was assumed. In order to demonstrate the applicability of the presented solution strategy to a large structure, a sector corresponding to one twelfth of the structure was studied in the present work as shown in Figure 15(b). The studied finite element model had a total height of 20 m. In the finite element model, all the nodes at the top of the shaft were constrained in the vertical direction, and the nodes along the radial symmetry edges were constrained in the hoop direction. The structure was assumed supported on soft soil, so that the vertical load could be applied as a constant outer pressure on the bottom slab.

Based on results from LFEA, the structure was designed with a special post-processor and non-linear sectional design software (Brekke et al., 1994) according to NS 3473 and EN-ISO 19903 (CEN, 2006; Norges Standardiseringsforbund, 2003). Only the dead weight of the concrete, the external and internal static water pressure and the total vertical load from the topside were considered in the present work in order to be able to reduce the complexity of the problem. The structure was designed for the applicable load combinations in the operation phase in the ultimate limit state.

The resulting reinforcement amounts from the non-linear sectional design were transferred back to the finite element model used in the NLFEA, and were modelled similarly as in the benchmark analyses described above. It should be noted that the complete structure could easily have been modelled, analysed and designed, but due to the symmetry with respect to load and geometry, and due to the mechanism of load transfer in circular shafts, a limited amount of information would have been gained compared to the smaller model that was used.

In a real design situation other static and dynamic loads and other limit states will require global modelling of the complete structure and are expected to have significant influence on the required shell thicknesses and reinforcement amounts. Also, the reinforcement amounts are normally adjusted in local areas due to e.g. constructability, continuity in reinforcement layout and required anchorage. However, in the present work, only the required amounts found directly from the ultimate limit design checks

were included.

A combination of local bending moments and transverse shear forces, and global membrane forces, results in a relatively complex distribution of internal sectional forces. The vertical load is transferred through the upper parts of the shaft as vertical compressive forces. When approaching the caisson, the shaft is subjected to additional local bending in the vertical direction, compressive forces in the hoop direction and transverse shear forces. The ribs provide stiffness to the caisson, and ensures that the caisson deforms as one unit, and that the vertical load is carried as a combination of global bending in the hoop and radial direction. The ribs are subjected to in-plane forces, while the top and bottom slab and the outer wall and the lower parts of the shaft within the caisson are subjected to in-plane forces, bending moments in two principal directions and transverse shear forces. Because the structure was assumed completely waterfilled, the internal and external water pressure mainly resulted in a slight prestressing of the structure due to the difference in internal and external area for load application.

In the NLFEA the dead weight of the concrete and the internal and external water pressure was first applied in five load steps, before the total load from the topside was applied in 40 load steps. It should be noted that in the present paper it was not attempted to perform a reliability assessment of the structure; the materials were assigned their characteristic strengths and the loads were applied with their characteristic intensities. Ideally, the results from the NLFEA should have been compared to experimental results, but for obvious reasons, no relevant results are available for such structures. Instead it would be valuable to study the difference in calculated response between a LFEA and a NLFEA, since the design is based on the former, and a possible global reliability assessment would be based on the latter. Hence, the global and local structural effects of material non-linearity are presented in the following comparing results from LFEA and NLFEA following the same load histories. The deformed shapes in the final load step of the LFEA and NLFEA shown in Figure 16 are provided as physical evidence for the discussion.

At 37.5% and 40% of the total vertical load, $F_{\mathrm{z,ext}}$, cracks appeared on the outer and inner face of the central parts of the bottom slab. The cracks resulted in a translation of the neutral axis in the central parts of the bottom slab, an elongation of the midplane and the significant radial displacement of the joint between the shaft and the bottom slab that can be seen in Figure 16(b). This effect, known in the literature as the *compressive membrane effect*, gave a reduction of the radial resultant tensile forces in section 1-1 in the central parts of the bottom slab as shown in Figure 17(a), but also an increase in hoop tension in the lower parts of the shaft, the outer wall and the rest of the bottom slab.

From 52.5% to 67.5% of the total vertical load, cracks appeared at the outer face of the bottom slab along the rib, the inner face of the bottom slab along the radial symmetry edge and in lower parts of the shaft along the rib. The cracking in the bottom slab led to a compressive membrane effect in hoop direction, slightly reducing the hoop tension in the bottom slab. The cracking in the shaft reduced the stiffness of the shaft, leading to a reduction of horizontal forces transferred from the rib to the shaft and a slight redistribution of global bending of the caisson from radial direction in section 3-3 to hoop direction in section 2-2 as shown in Figures 17(b) and 17(c). The global resultant moments M_{hoop} and M_{rad} were calculated by summing the moment contributions around the mid-height of the caisson from the nodal forces in hoop direction in section 2-2 and radial direction in section 3-3 respectively. Due to the reduction of horizontal force transfer from the rib to the shaft, the tensile and

compressive resultants due to global radial bending of the caisson were localized in the bottom and top slab respectively. As the vertical load was further increased to the characteristic level, cracking propagated in the described cracked areas, and only minor cracking appeared in the outer wall and in the lower parts of the rib close to the joint between the shaft and the bottom slab. The reinforcement did not yield in any direction. The compressive membrane effect in the two directions in the bottom slab resulted in crack closure, where some of the closed cracks remained closed during the rest of the load application, but some also reopened. At the final load level 11757 cracks had appeared in the structure, of which 153 were closed.

Due to the global force redistribution, a change of local behaviour was observed, e.g. the principal compressive stress, σ_3, in the shaft above the top slab increased from -23.5 MPa to -25.7 MPa, and σ_3 in the rib close to the joint between the shaft and the top slab increased from -10.0 MPa to -10.6 MPa. A beneficial reduction of tensile forces in the bottom slab thus came with the expense of increased compressive stresses in the shaft and the rib.

6. Discussion

The level of detail which is required for the material model depends on the phenomena that are to be studied in the analysis. In the present work, the ultimate load capacity was sought, and for this application the simple material models for concrete and reinforcement was appropriate. The results were supporting the conclusions from Engen et al. (2015) advising a shift of the attention from a detailed description of the post-cracking tensile behaviour to a rational description of the pre-cracking compressive behaviour of concrete in analyses where large finite elements are used. The assumed brittleness in tension and compression was considered a useful simplification which resulted in a material model with only one material parameter needed. If on the other hand a tensile softening relation based on crack bandwidth and fracture energy was used, results from Bazant and Oh (1983) and Hendriks et al. (2017) show that the element size should be limited to 100-400 mm depending on the cylinder strength in order to avoid snap-backs in the constitutive relation. The limiting values correspond to a sudden vertical drop in the stress-strain relation upon cracking (Bazant and Oh, 1983). Because the size of the elements used in the present work was in the order of these limiting values and the results indicated insignificant sensitivity to finite element size, the simplified brittle behaviour was justified. With the scope of the present work being focused on large *reinforced* concrete structures, the brittle degradation of one local point is not expected to significantly influence the ultimate load capacity, since the stresses released due to cracking of the concrete are directly supported by the reinforcement. If however, lightly reinforced or unreinforced concrete was studied, a more detailed description of the post-cracking tensile behaviour might become necessary.

Although not presented in detail in the present paper, the tolerances of the convergence criteria and the maximum number of iterations were observed not to significantly influence the predicted global behaviour, but influenced which load was treated as the predicted capacity in the benchmark analyses. This result indicates that the solutions were converged to a *stable* state close to equilibrium, and that the remaining force unbalance in unconverged load steps might be due to local self-equilibrating unbalances as discussed by Bergan and Holand (1979). In most of the load steps of the presented NLFEA, the energy convergence criterion was governing, i.e. it was satisfied before the force criterion, even though a tighter tolerance was used for the energy criterion.

The two criteria are fundamentally different, and the tolerances are not directly comparable, but the results indicate that different criteria require different tolerances in order to obtain comparative levels of accuracy, and that it is important to state both the selected tolerance and the mathematical expression of the criterion when results from NLFEA are presented.

The cylinder strength reported in the references was used directly as the only input material parameter for the concrete material model in the benchmark analyses, and was not calibrated in order to improve the results. This was considered particularly important in engineering applications where the results are not known on beforehand. The results from the benchmark analyses did not show exact crack patterns, but the failure modes and the ultimate limit loads were close to what was experimentally obtained. Finite elements of the size that was used in the present study are typically in the order of the crack spacing and localized crack patterns can not be expected.

The results from the NLFEA of the large shell structure show that a global analysis is required for a realistic assessment of such structures. If only local analyses were performed, the analyst should pay close attention to the applied boundary conditions. If the central part of the bottom slab was modelled locally, the compressive membrane effect could be overestimated if the slab was fully constrained in the radial direction. Also, if only the rib was modelled, the effect of redistribution of resultants from global bending could not be predicted, and too large horizontal force transfer from the rib to the shaft might be predicted, which could lead to an overestimation of crack widths and stresses in the horizontal reinforcement. With a solution time of approximately 6 s per equilibrium iteration, the solution strategy presented in the present paper is considered applicable for NLFEA of large concrete structures in the design phase.

7. Conclusions

Development of a solution strategy for NLFEA should as a minimum include the four steps 1) definition, 2) verification, 3) validation and 4) demonstration of applicability. This contribution complements findings published by the authors in two separate publications (Engen et al., 2015, 2017). In spite of relatively simple material models and large finite elements, the results from the present work indicate that the presented solution strategy has a low modelling uncertainty and a low element size and load step size dependency. With the presented solution strategy, the practising engineer is equipped with an efficient tool for performing detailed assessments of the ultimate load capacity and the structural reliability of new and existing large reinforced concrete structures. This will be elaborated on in the further work of the present research project.

Acknowledgments

The work presented in this paper is part of an industrial PhD funded by Multiconsult ASA and The Research Council of Norway. Morten Engen thanks his supervisors and all colleagues in the Marine Structures Department at Multiconsult for valuable discussions and particularly Per Horn, former Senior Vice President of Multiconsult, for having the courage to initiate the research project.

References

H. Bark, G. Markou, C. Mourlas, and M. Papadrakakis. Seismic assessment of a 5-storey retrofitted rc building. In *ECCOMAS Congress 2016, VII European Congress on Computational Methods in Applied Sciences and Engineering, Crete Island, Greece, 5-10 June 2016*, 2016.

J. Barlow. More on Optimal Stress Points - Reduced Integration, Element Distortions and Error Estimations. *International Journal for Numerical Methods in Engineering*, 28:1487–1504, 1989.

J. Barlow. Optimal Stress Locations in Finite Element Models. *International Journal for Numerical Methods in Engineering*, 10:243–251, 1976.

K.-J. Bathe, J. Walczak, A. Welch, and N. Mistry. Nonlinear Analysis of Concrete Structures. *Computers & Structures*, 32(3/4):563–590, 1989.

Z. P. Bazant and B. H. Oh. Crack band theory for fracture of concrete. *Materials and Structures*, 16(3):155–177, 1983.

C. Bédard and M. D. Kotsovos. Application of NLFEA to Concrete Structures. *Journal of Structural Engineering*, 111(12):2691–2707, 1985.

B. Belletti, C. Damoni, and M. A. N. Hendriks. Development of guidelines for nonlinear finite element analyses of existing reinforced and pre-stressed beams. *European Journal of Environmental and Civil Engineering*, 15(9)(9):1361–1384, 2011.

B. Belletti, C. Damoni, J. A. den Uijl, M. A. N. Hendriks, and J. Walraven. Shear resistance evaluation of prestressed concrete bridge beams: *fib* Model Code 2010 guidelines for level IV approximations. *Structural Concrete*, 14(3):242–249, 2013.

B. Belletti, C. Damoni, M. A. N. Hendriks, and A. de Boer. Analytical and numerical evaluation of the design shear resistance of reinforced concrete slabs. *Structural Concrete*, 15(3): 317–330, 2014.

B. Belletti, M. Pimentel, M. Scolari, and J. C. Walraven. Safety assessment of punching shear failure according to the level of approximation approach. *Structural Concrete*, 16(3): 366–380, 2015.

P. G. Bergan and I. Holand. Nonlinear finite element analysis of concrete structures. *Computer Methods in Applied Mechanics and Engineering*, 17/18(2):443–467, 1979.

D.-E. Brekke, E. Åldstedt, and H. Grosch. Design of Offshore Concrete Structures Based on Postprocessing of Results from Finite Element Analysis (FEA): Methods, Limitations and Accuracy. In *Proceedings of the Fourth (1994) International Offshore and Polar Engineering Conference*, 1994.

B. Bresler and A. C. Scordelis. Shear Strength of Reinforced Concrete Beams. *Journal of the American Concrete Institute*, 60(1):51–74, 1963.

V. Cervenka and K. H. Gerstle. Inelastic Analysis of Reinforced Concrete Panels: Experimental Verification and Application. *IABSE Publications*, 32:31–45, 1972.

D. M. Cotsovos. *Numerical Modelling of Structural Concrete under Dynamic (Earthquake and Impact) Loading*. PhD thesis, Imperial College London, 2004.

D. M. Cotsovos and M. N. Pavlovic. Simplified FE model for RC structures under earthquakes. *Proceedings of the ICE - Structures and Buildings*, 159(SB2):87–102, 2006.

R. de Borst and P. Nauta. Non-orthogonal cracks in a smeared finite element model. *Engineering Computations*, 2(1):35–46, 1985.

fib. Bulletin 45: Practitioner's guide to finite element modelling of reinforced concrete structures. International Federation for Structural Concrete (*fib*), 2008.

fib. Bulletin 50: Concrete structures for oil & gas fields. International Federation for Structural Concrete (*fib*), 2009.

fib. fib *Model Code for Concrete Structures 2010*. Ernst & Sohn, 2013.

M. Engen, M. A. N. Hendriks, J. A. Øverli, and E. Åldstedt. Application of NLFEA in the Design of Large Concrete Structures. In *Proceedings of the XXII Nordic Concrete Research Symposium, Reykjavik, Iceland 2014*, 2014.

M. Engen, M. A. N. Hendriks, J. A. Øverli, and E. Åldstedt. Solution strategy for non-linear

Finite Element Analyses of large reinforced concrete structures. *Structural Concrete*, 16(3): 389–397, 2015.

M. Engen, M. A. N. Hendriks, J. Köhler, J. A. Øverli, and E. Åldstedt. A Quantification of the Modelling Uncertainty of Non-linear Finite Element Analyses of Large Concrete Structures. *Structural Safety*, 64:1–8, 2017.

G. C. Ernst, G. M. Smith, A. R. Riveland, and D. N. Pierce. Basic Reinforced Concrete Frame Performance Under Vertical and Lateral Loads. *ACI Journal*, 70(4):261–269, 1973.

CEN. EN ISO 19903: Petroleum and natural gas industries. Fixed concrete offshore structures, 2006.

F. González Vidosa. *Three-dimensional finite element analysis of structural concrete under static loading*. PhD thesis, University of London, 1989.

F. González Vidosa, M. D. Kotsovos, and M. N. Pavlovic. On the Numerical Instability of the Smeared-Crack Approach in the Non-Linear Modelling of Concrete Structures. *Communications in Applied Numerical Methods*, 4(6):799–806, 1988.

F. González Vidosa, M. D. Kotsovos, and M. N. Pavlovic. Three-dimensional non-linear finite-element model for structural concrete. Part 1: main features and objectivity study. *Proceedings of the ICE - Structures and Buildings*, 91:517–544, 1991a.

F. González Vidosa, M. D. Kotsovos, and M. N. Pavlovic. Three-dimensional non-linear finite-element model for structural concrete. Part 2: generality study. *Proceedings of the ICE - Structures and Buildings*, 91:545–560, 1991b.

M. A. N. Hendriks, A. de Boer, and B. Belletti. Guidelines for Nonlinear Finite Element Analysis of Concrete Structures. Rijkswaterstaat Centre for Infrastructure, Report RTD:1016-1:2017, 2017.

I. Jelic, M. N. Pavlovic, and M. D. Kotsovos. Performance of structural-concrete members under sequential loading and exhibiting points of inflection. *Computers and Concrete*, 1(1): 99–113, 2004.

M. D. Kotsovos. A mathematical description of the strength properties of concrete under generalized stress. *Magazine of Concrete Research*, 31(108):151–158, 1979a.

M. D. Kotsovos. Fracture processes of concrete under generalised stress states. *Materials and Structures*, 12(72):431–437, 1979b.

M. D. Kotsovos. A mathematical model of the deformational behavior of concrete under generalised stress based on fundamental material properties. *Materials and Structures*, 13(76):289–298, 1980.

M. D. Kotsovos. A fundamental explanation of the behaviour of reinforced concrete beams in flexure based on the properties of concrete under multiaxial stress. *Materials and Structures*, 15(90):529–537, 1982.

M. D. Kotsovos. Concrete. A brittle fracturing material. *Materials and Structures*, 17(98): 107–115, 1984.

M. D. Kotsovos and M. N. Pavlovic. *Structural Concrete: Finite-element analysis for limit-state design*. Thomas Telford, 1995.

M. D. Kotsovos and K. V. Spiliopoulos. Modelling of crack closure for finite-element analysis of structural concrete. *Computers & Structures*, 69(3):383–398, 1998.

M. D. Kotsovos, M. N. Pavlovic, and D. M. Cotsovos. Characteristic features of concrete behaviour: Implications for the development of an engineering finite-element tool. *Computers and Concrete*, 5(3):243–260, 2008.

I. D. Lefas, M. D. Kotsovos, and N. N. Ambraseys. Behaviour of Reinforced Concrete Structural Walls: Strength, Deformation Characteristics, and Failure Mechanism. *ACI Structural Journal*, 87(1):23–31, 1990.

G. C. Lykidis and K. V. Spiliopoulos. 3D Solid Finite-Element Analysis of Cyclically Loaded RC Structures Allowing Embedded Reinforcement Slippage. *Journal of Structural Engineering*, 134(4):629–638, 2008.

G. Markou, R. Sabouni, F. Suleiman, and R. El-Chouli. Full-Scale Modeling of the Soil-Structure Interaction Problem Through the use of Hybrid Models (HYMOD). *International Journal of Current Engineering and Technology*, 5(2):885–899, 2015.

G. Markou and M. Papadrakakis. Computationally efficient 3D finite element modeling of RC structures. *Computers and Concrete*, 12(4):443–498, 2013.

C. Mourlas, M. Papadrakakis, and G. Markou. Accurate and efficient modeling for the cyclic behavior of rc structural members. In *ECCOMAS Congress 2016, VII European Congress on Computational Methods in Applied Sciences and Engineering, Crete Island, Greece, 5-10 June 2016*, 2016.

Norges Standardiseringsforbund. NS 3473.E: Design of concrete structures. Design and detailing rules. 6th edition, September 2003.

M. Pimentel, E. Brühwiler, and J. A. Figueiras. Safety examination of existing concrete structures using the global resistance safety factor concept. *Engineering Structures*, 70: 130–143, 2014.

P. J. Roache. Verification of Codes and Calculations. *AIAA Journal*, 36(5):696–702, 1998.

J. G. Rots. *Computational modeling of concrete fracture*. PhD thesis, Technische Universiteit Delft, 1988.

J. G. Rots and J. Blaauwendraad. Crack models for concrete: Discrete or smeared? Fixed, multidirectional or rotating? *Heron*, 34(1):1–59, 1989.

H. Schlune, M. Plos, and K. Gylltoft. Safety formats for non-linear analysis of concrete structures. *Magazine of Concrete Research*, 64(7):563–574, 2012.

J. C. Simo and M. S. Rifai. A Class of Mixed Assumed Strain Methods and the Method of Incompatible Modes. *International Journal for Numerical Methods in Engineering*, 29: 1595–1638, 1990.

J. C. Simo, F. Armero, and R. L. Taylor. Improved versions of assumed enhanced strain trilinear elements for 3D finite deformation problems. *Computer Methods in Applied Mechanics and Engineering*, 110:359–386, 1993.

K. V. Spiliopoulos and G. Ch. Lykidis. An efficient three-dimensional solid finite element dynamic analysis of reinforced concrete structures. *Earthquake Engineering and Structural Dynamics*, 35(2):137–157, 2006.

F. J. Vecchio. Non-linear finite element analysis of reinforced concrete: at the crossroads? *Structural Concrete*, 2(4):201–212, 2001.

F. J. Vecchio and S. Balopoulou. On the Nonlinear Behaviour of Reinforced Concrete Frames. *Canadian Journal of Civil Engineering*, 17(5):698–704, 1990.

F. J. Vecchio and M. B. Emara. Shear Deformations in Reinforced Concrete Frames. *ACI Structural Journal*, 89(1):46–56, 1992.

J. A. Øverli. A density-dependent failure criterion for concrete. *Construction and Building Materials*, 124:566–574, 2016.

K. J. Willam and E. P Warnke. Constitutive Model for the Triaxial Behaviour of Concrete. *IABSE reports of the working commissions*, 19:1–30, 1974.